



Li⁺ co-doping induced phase transition as an efficient strategy to enhance upconversion of La₂Zr₂O₇:Er,Yb nanoparticles

Santosh K. Gupta ^a, Maya Abdou ^b, Jose P. Zuniga ^b, Partha S. Ghosh ^c, Yuanbing Mao ^{d,*}

^a Radiochemistry Division, Bhabha Atomic Research Centre, Trombay, Mumbai, 400085, India

^b Department of Chemistry, University of Texas Rio Grande Valley, 1201 West University Drive, Edinburg, TX, 78539, USA

^c Materials Science Division, Bhabha Atomic Research Centre, Trombay, Mumbai, 400085, India

^d Department of Chemistry, Illinois Institute of Technology, 3105 South Dearborn Street, Chicago, IL, 60616, USA

ARTICLE INFO

Keywords:

Lanthanum zirconate
Pyrochlore
Lithium
Nanoparticles
Upconversion
Phase transition

ABSTRACT

The structural phase transition of materials is one of the most active research areas of solid state and materials chemistry in which atomic rearrangements tune fundamental physicochemical properties during the transition. In most cases, such transition requires high temperature, high pressure, or chemical doping. However, phase transition of complex metal oxides such as La₂Zr₂O₇ has not been studied to enhance the upconversion (UC) and downconversion luminescence of their rare-earth doped nanoparticles (NPs) to meet the demand of their broad applications in solar cells, bioimaging, water purification, etc. In this work, we have successfully co-doped Li⁺ into La₂Zr₂O₇:Er,Yb NPs to achieve phase transition from ideal ordered pyrochlore (OP) to disordered fluorite (DF) structure. We have confirmed this phase transition to endow UC enhancement from these NPs under 980 nm excitation. Specifically, the UC enhancement of the green and red emissions are 14- and 18-fold, respectively. Meanwhile, DFT calculations indicated that the position of Li atoms with respect to Er doping plays a decisive role in dictating the relative stability of DF and OP structures. To sum, it is expected that the idea provided in this work by realizing and understanding doping induced phase transition to enhance down/upconversion luminescence of NPs can be extended to other metal oxide systems.

1. Introduction

Structural phase transitions provide not only physical insight of materials but also induce interesting physical phenomena, especially optical and electrical ones [1–10]. Li⁺ ions can be easily incorporated into inorganic crystal lattice substitutionally or interstitially because of their small size [11]. So Li⁺ ion doping is expected to reduce or remove the symmetry of the crystal field around rare-earth (RE) dopants in upconversion (UC) nanoparticles (NPs), which leads to enhance UC intensity [12]. More specifically, Li⁺ co-doping has been reported to enhance both UC and downconversion emission intensity by virtue of reducing lattice strain, taking care of charge compensation, and acting as a sensitizer for energy transfer [11,13]. For example, Singh et al. have reported that the incorporation of Li⁺ ions modified the crystal field of Y₂Ti₂O₇ around the Er³⁺ ions and enhanced UC intensity [13]. Zhao et al. have improved the UC of NaYF₄:Yb³⁺,Tm³⁺ nanocrystals via Li⁺ doping. They attributed the obtained results to the lowering of symmetry around Tm³⁺ ions and the improvement of crystallinity of the

nanocrystals after Li⁺ doping [14]. Zhao and his group reported that Li⁺ co-doped GdF₃:Er³⁺,Yb³⁺ nanoparticles showed improved red UC intensity due to the reduction of local crystal field symmetry around Er³⁺ ion after Li⁺ doping [15]. Nannuri et al. and Shang et al. have improved UC intensity of NaYF₄:Er,Yb bulk crystal with cubic to hexagonal phase transition induced by annealing temperature and reaction time, respectively [3,4]. These treatments cause an increase of their crystal size, which limits their biological imaging applications. Du et al. have improved UC intensity of the same material by Cu²⁺ co-doping, which induced cubic to hexagonal phase transition [2]. Xu et al. reported UC intensity enhancement by Mn²⁺ induced phase transition from orthorhombic KLu₂F₇ to cubic KLu₃F₁₀ [7]. The same group also enhanced UC intensity by a phase transition from anisotropic (orthorhombic KLu₂F₇:Yb³⁺/Er³⁺) to isotropic (cubic KLu₃F₁₀:Yb³⁺/Er³⁺) induced by doping similar ionic charge ions such as Gd³⁺ and Nd³⁺ [8]. All these discussions indicated that most of the studied materials were fluoride-based compounds, specifically NaYF₄. There has not been much progress in exploring this approach to new kinds of materials to open up new

* Corresponding author.

E-mail address: ymao17@iit.edu (Y. Mao).

dimensions in materials science. Fluorides as hosts have the advantage of low phonon energy, but their chemical stability and associated toxicity are serious issues [16,17]. Moreover, co-dopants in most of the above studies, which favored phase transition, were either divalent or trivalent ions. There is barely any report on lithium induced phase transition to induce UC enhancement. Meanwhile, it was reported that Li^+ doping induces structural phase transition in $\text{Bi}_{0.5}\text{Na}_{0.5}\text{TiO}_3$ and VO_2 with improved ferroelectric and electronic properties [1,6].

Photon UC is a process of generating high energy emission from low energy absorption via multiple photon absorption [18,19]. With the advent of nanotechnology, UC nanoparticles (UCNPs) have become a subject of intense research directed towards multifunctional applications [18,20,21]. Among UCNPs, RE doped materials have obvious advantages, particularly in the areas of solar cells, photodynamic therapy, temperature sensors, and bioimaging [14,20–22]. These advantages include narrow emission, high color purity, large anti-Stokes shifts, multicolor emission, biocompatibility, and photostability [20]. UC emission of RE doped UCNPs is strongly dependent on the probability of intra-configurational f-f transitions. Exploiting RE doped UCNPs for above mentioned applications has not generated desirable results because of the low UC intensity associated with f-f transitions of RE ions. The intra-configurational f-f transitions of RE ions are strongly influenced by strength and symmetry of local crystalline field of RE ions [23]. Several techniques have been adopted to enhance UC intensity such as crystal field modification, co-doping, sensitizing, surface coating, core/shell strategy, etc. [14,24,25] The distance between RE ions, their relative spatial location, their local coordination number, and their local environment are determined by host lattice. In addition, an ideal host matrix should be transparent in the spectral range of interest, have high optical damage threshold, low phonon energy, and be chemically stable. Therefore, host matrices have strong influence on UC efficiency of UCNPs and should be properly selected.

Lanthanum zirconate $\text{La}_2\text{Zr}_2\text{O}_7$ (LZO) has a pyrochlore structure with a wide bandgap, high structural stability, high dielectric constant, low phonon energy, optimum refractive index, ability to easily accommodate lanthanide ions at both La^{3+} and Zr^{4+} sites, high thermal stability, etc. [26,27] It has been reported to undergo $\text{A}_2\text{B}_2\text{O}_7$ -type ordered pyrochlore (OP, Fd-3m) phase transition to disordered fluorite phase (DF, Fm-3m) or vice versa ($\text{DF} \rightleftharpoons \text{OP}$) under high temperature, high pressure, ionizing radiation, and/or via chemical doping [28–30]. Radius ratio (r_A/r_B) plays a decisive part in this phase transition. OP is the stable phase when the value of radius ratio is >1.46 whereas the DF phase is the stable one in case of r_A/r_B is less than 1.46. It has been observed in literature that aliovalent doping of $\text{A}_2\text{B}_2\text{O}_7$ -type pyrochlores induces pyrochlore-to-fluorite/cotunnite structural transition [30,31]. Each phase has its own advantages: the OP phase is found to be suitable for sensing, scintillation, and thermal barrier coatings, whereas the DF phase is found to be ideal for nuclear waste host, ionic conductor, etc. [28,30,32,33].

In this work, we studied Er,Yb-doped LZO NPs which showed efficient NIR to visible UC. More importantly, we co-doped Li^+ ions into the Er,Yb-doped LZO NPs and observed UC emission intensity enhancement virtually via order to disorder phase transition of the LZO host for the first time. We believe that this phase transition is driven by two processes: (i) easy intercalation of Li^+ ions in LZO network and (ii) nanodimension of the LZO NPs with short diffusion path to reduce the kinetics barrier of such transition [34]. Furthermore, density functional theory (DFT) calculations were conducted to validate our experimental data. Based on DFT data, it was inferred that Li^+ co-doping with certain bonding positions around Er^{3+} ions favors the formation of disorder LZO phase, which is responsible for the enhancement of UC intensity.

2. Experimental

2.1. Synthesis

Lanthanum nitrate hexahydrate ($\text{La}(\text{NO}_3)_3 \cdot 6\text{H}_2\text{O}$, 99.0%), zirconium oxynitrate pentahydrate ($\text{ZrO}(\text{NO}_3)_4 \cdot 5\text{H}_2\text{O}$, 99.0%), erbium nitrate pentahydrate ($\text{Er}(\text{NO}_3)_3 \cdot 5\text{H}_2\text{O}$, 99.0%), ytterbium nitrate pentahydrate ($\text{Yb}(\text{NO}_3)_3 \cdot 5\text{H}_2\text{O}$, 99.0%), potassium nitrate (KNO_3 , 99.9%), sodium nitrate (NaNO_3 , 98%), and lithium nitrate (LiNO_3 , 98%) were obtained commercially from Sigma Aldrich with no further purification.

The synthesis included a two-step protocol involving a coprecipitation process followed by the molten salt synthesis (MSS) [27,30]. Stoichiometric amounts of starting reactants were used. Specifically, in the first step, $5(1-x-y)$ mmol of $\text{La}(\text{NO}_3)_3 \cdot 6\text{H}_2\text{O}$, 5 mmol $\text{ZrO}(\text{NO}_3)_4 \cdot 5\text{H}_2\text{O}$, $5x$ mmol $\text{Er}(\text{NO}_3)_3 \cdot 5\text{H}_2\text{O}$ and $5y$ mmol $\text{Yb}(\text{NO}_3)_3 \cdot 5\text{H}_2\text{O}$ were weighted and dissolved in 200 mL of deionized water ($18.2 \text{ M}\Omega$ at 25°C). The aqueous solution of the starting reactants was mixed for 30 min using a magnetic stirring bar. Then, the solution was titrated with 200 mL of 10% diluted ammonium hydroxide solution (NH_4OH , 28–30%) in a time range of 2 h. A cloudy precipitate formed at the bottom of the beaker. The precipitate was collected through vacuum filtration, washed till the pH value of the filtrate solution was neutral, and then dried overnight in air at room temperature. This resulted in a final single-source complex precursor $(1-x-y)\text{La}(\text{OH})_3 \cdot x\text{Er}(\text{OH})_3 \cdot y\text{Yb}(\text{OH})_3 \cdot \text{ZrO}(\text{OH})_2 \cdot n\text{H}_2\text{O}$. The concentration of Er^{3+} and Yb^{3+} is optimized based on our previous work, i.e. $x = 3\%$ and $y = 20\%$ [35].

The second part of the protocol involved the employment of the MSS method. Sodium nitrate and potassium nitrate were selected as the flux salts. The obtained single-source complex precursor was mixed with them in a 1:30:30 stoichiometric ratio. The mixture was placed in a mortar and ground finely with the addition of acetone for about 10–30 min. The resulting mixture was then annealed at 650°C for 6 h in a box furnace with ramp-up and ramp-down rates of $5^\circ\text{C}/\text{min}$. The final product was washed several times with distilled water and dried in the oven at 90°C overnight.

To improve the UC luminescence efficiency of the LZO:3%Er,20%Yb NPs, we further co-doped them with Li^+ ions. In this study, the Li^+ co-doped LZO:3%Er,20%Yb NPs were synthesized similarly via the MSS process described above with Li^+ concentrations of 1, 2, 5, 10, and 15%. The annealing temperature and time were kept the same as used in the preceding synthesis, i.e. 650°C and 6 h. For simplicity, these new samples are denoted as LZO:ErYb-0Li, LZO:ErYb-1Li, LZO:ErYb-2Li, LZO:ErYb-5Li, LZO:ErYb-10Li, and LZO:ErYb-15Li, respectively.

2.2. Characterization

The structural and morphological properties of the obtained samples were extensively studied using powder X-ray diffraction (XRD), scanning electron microscopy (SEM), and Raman spectroscopy. XRD patterns were recorded using a Rigaku Miniflex X-ray Diffractometer with a $\text{Cu K}_{\alpha 1}$ radiation ($\lambda = 0.15406 \text{ nm}$, 30 kV and 15 mA), where the scanning mode was set to 2-theta, with scanning range from 10° to 90° , scanning step size of 0.05° , and scanning rate of 2° min^{-1} . Raman spectra were obtained with a Bruker SENTERRA Raman spectrometer (Bruker Optics SENTERRA R200) that uses solid state laser (785 nm) with 100 mW power. A Carl Zeiss sigma VP scanning electron microscopy equipped with a field emission gun operated at 5 kV (FESEM) was used to collect SEM images of the samples. PL emission were recorded using an Edinburgh Instrument FLS 980 fluorimeter system equipped with both a pulsed and a steady state xenon lamp source, with a pulse frequency range of 1–100 Hz and an equipped with MDL-III-980-2W Class IV laser. The UC properties were investigated using a 980 nm laser.

2.3. DFT Calculations

All the electronic structure calculations of OP and DF structures of

LZO host (with/without Er, Yb and Li doping) were performed using a plane wave based spin-polarized density functional theory (DFT) as implemented in Vienna Ab initio Simulation Package (VASP) [36,37]. The electron-ion interaction was described by projector augmented wave (PAW) potential which includes the valence states of La ($5s^25p^65d^16s^2$ - 11 valence electrons), Zr ($4s^24p^65s^24d^2$ - 12 valence electrons), O ($2s^22p^4$ - 6 valence electrons), Er ($5s^26s^25p^66d^1$ - 9 valence electrons) and Yb ($5s^26s^25p^6$ - 8 valence electrons) [38]. The generalized gradient approximation (GGA) with Perdew-Burke-Ernzerhof (PBE) parameterization was used for the exchange-correlation part [39]. A Monkhorst-Pack k-space mesh of $4 \times 4 \times 4$ in reciprocal space for the Brillouin zone integration was used for the 88 atoms cells [40]. The plane wave cutoff energy (E_{cut}) of 600 eV for basis set was used throughout the simulation. The optimization was carried out to get converged values for E_{cut} and k-point meshes which ensure convergence of total energy to within a precision 0.05 meV/atom. The cohesive energy of LZO were optimized with respect to volume (or lattice parameter) and atomic positions using conjugate gradient algorithm until the residual forces and stress in the equilibrium geometry were of the order of 0.005 eV/Å and 0.01 GPa, respectively. The final calculation of total electronic energy and density of states (DOS) were performed using the tetrahedron method with Blöchl corrections [41].

All the calculations were performed on an 88-atom supercell for both OP and DF. For OP, an 88-atom supercell was a standard $2 \times 2 \times 2$ cell of 22 atom primitive cell. For DF, an 88-atom Special Quasi-random Structure (SQS) for the fully disordered $(A_{1/2}B_{1/2})(O_{7/8}V_{1/8})_2$ structure was used. These structures were generated using Monte-Carlo simulated annealing technique [42]. In order to study the effect of Er/Yb/Li doping, each of one Er/Yb/Li atom was replaced in place of La/Zr site in the 88-atom supercell.

3. Results and discussion

3.1. SEM images

The SEM images of our MSS synthesized LZO:Er,Yb NPs with different Li^+ co-doping concentrations clearly showed the formation of fine monodispersed nanograins (Fig. 1). These nanograins are mostly spherical particles in the range of 15–50 nm with some agglomerations. Moreover, the particle size of these NPs gradually increases from 15 nm to 50 nm as the Li^+ co-doping level increases from 0 to 15%, similar to the calculated crystalline size from the XRD data shown below. The size evolution of the Li^+ co-doped LZO:Er,Yb NPs can be ascribed to surface charge modification influenced by the Li^+ co-dopant, which has previously been reported on $Li^+/Mn^{2+}/Gd^{3+}$ co-doped $NaYF_4$ nanocrystals [5,43,44].

3.2. XRD patterns

XRD patterns of the LZO:Er,Yb NPs with different Li^+ co-doping concentrations (Fig. 2a) visibly show the establishment of single phase without any other peaks from possible impurities. The narrow peaks indicate high crystallinity of all LZO:Er,Yb NPs either Li^+ co-doped or not. Li^+ co-doping does not change the parent XRD pattern of the LZO:Er,Yb NPs indicating no change in the sample's purity. It is difficult to distinguish the DF and OP phases based on XRD data for the LZO:Er,Yb samples with or without Li^+ co-doping due to the proximity of these two structures [30].

The most intense XRD peak (222) shifts to higher 2θ value as the Li^+ co-doping level increases from 0 to 5% whereas the same peak shifts to lower 2θ value as the Li^+ co-doping level further increases from 5% to 15% (Table 1). The former trend can be attributed to the substitution of small Li^+ ions at La^{3+} and Zr^{4+} sites, which leads to the shrinkage of the LZO lattice. Accordingly, there is a reduction of the interplanar spacing d and the diffraction 2θ angle shifts to higher value. Therefore, Li^+ ions have been successfully co-doped into LZO host lattice up to 5% co-

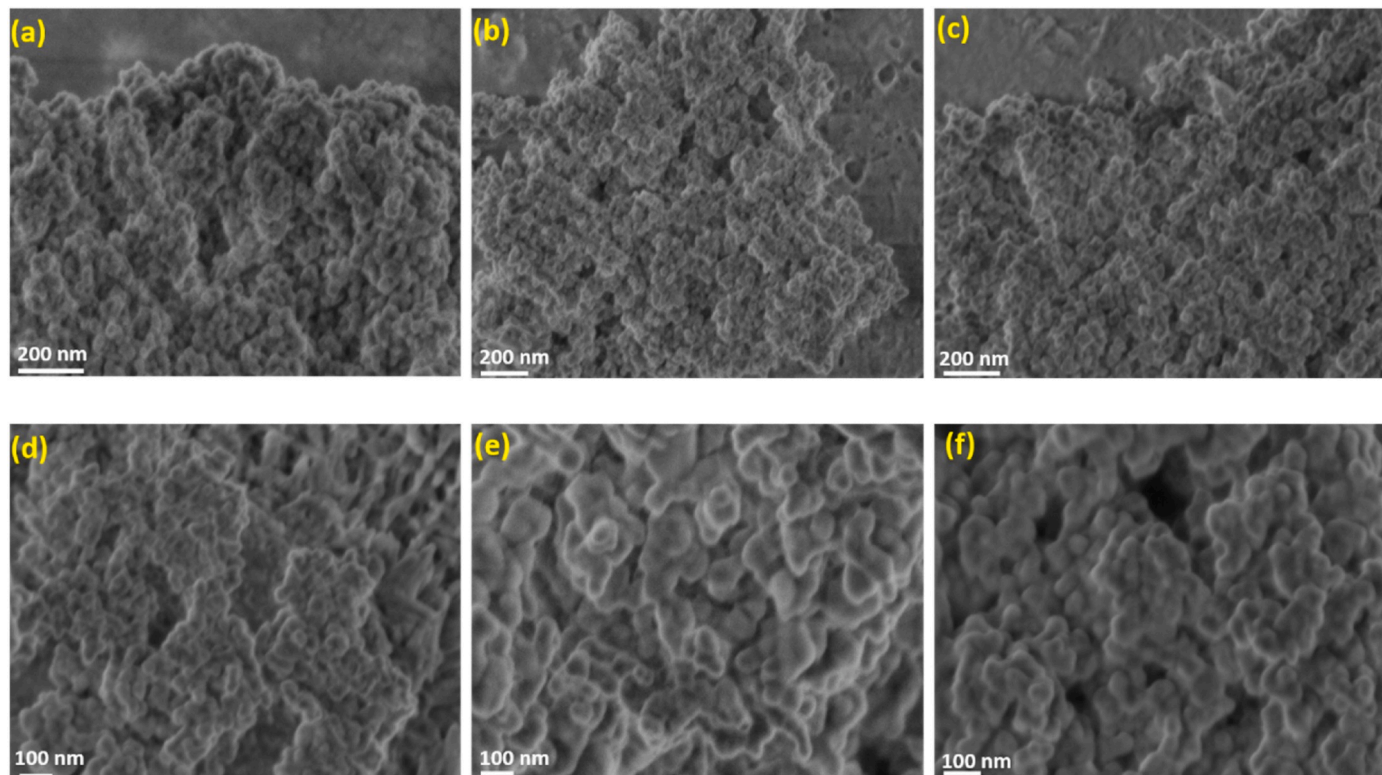


Fig. 1. SEM images of the LZO:Er,Yb NPs co-doped with different Li^+ concentrations: (a) 0%, (b) 1%, (c) 2%, (d) 5%, (e) 10%, and (f) 15%.

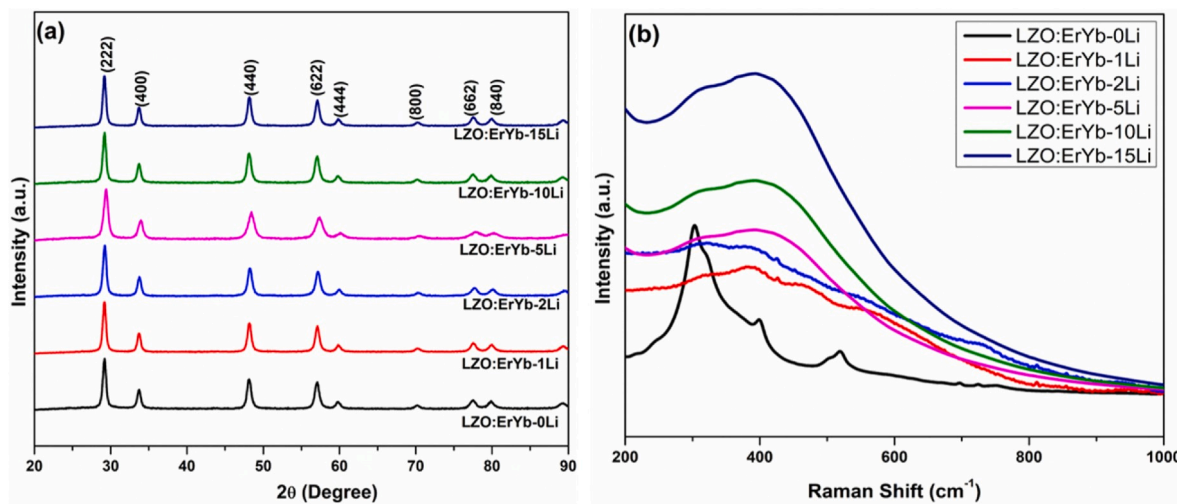


Fig. 2. (a) XRD patterns and (b) Raman spectra of the LZO:Er,Yb NPs co-doped with different Li⁺ concentrations.

Table 1

The 2-theta value of the most intense XRD peak (222) and its FWHM along with the calculated crystallite size and lattice parameter of the LZO:Er,Yb:x%Li (x = 0–15) NPs.

UCNPs	2θ (°)	FWHM (β)	Crystalline size (nm)	Lattice parameter <i>a</i> (Å)
LZO:ErYb-0Li	29.29	29.18	11.63	10.59
LZO:ErYb-1Li	29.42	29.01	16.37	10.60
LZO:ErYb-2Li	29.56	28.89	20.83	10.58
LZO:ErYb-5Li	29.68	28.69	23.90	10.56
LZO:ErYb-10Li	29.16	28.46	25.86	10.55
LZO:ErYb-15Li	29.04	28.37	31.83	10.57

doping level [43]. On the other hand, when the Li⁺ co-doping level is larger than 5%, the extra Li⁺ ions start occupying interstitial positions and the LZO lattice expands. Consequently, the interplanar spacing *d* value increases and the 2θ shifts to smaller value [14]. Based on these discussions, Li⁺ ions substitute lattice positions when its co-doping level $\leq 5\%$ and start occupying interstitial sites when its co-doping level is higher than 5% (and up to 15% in this study). The substitution of Li⁺ ions at La³⁺/Zr⁴⁺ sites or the occupation of interstitial positions can modify the local symmetry and crystal field around the activator Er³⁺ ions, which are expected to affect the UC emission properties of the LZO:Er,Yb NPs. Similar results have been observed in Li⁺ co-doped NaYF₄:Yb,Er/Tm and ABO₄:Yb,Er (A = Ca/Sr and B = W/Mo) nanocrystals [14, 43, 45].

Crystallite size and crystallinity of the Li⁺ co-doped LZO:Er,Yb NPs have been obtained from the full width half maxima (FWHM) of their XRD patterns, more specifically, the most intense (222) peak. As the Li⁺ co-doping level increases, the FWHM decreases. This phenomenon suggests increasing crystallinity. Moreover, the crystallite size of the Li⁺ co-doped LZO:Er,Yb NPs has been calculated using the Debye-Scherer formula:

$$d = \frac{k\lambda}{\sqrt{(B_s^2 - B_M^2)} \cos\theta} \quad (1)$$

where *d* is the calculated crystallite size, *λ* is the wavelength of the X-ray radiation used for the XRD patterns, *θ* is the angle of the corresponding Bragg reflection, which was fitted to calculate the FWHM. *B* is the

FWHM in radian. *K* is a Scherer constant 0.94 based on cubic crystal structure. The *B_M* was calculated using the FWHM value of the nearby highest intensity peak of pure silicon. In our study, the FWHM was determined based on the XRD peak (222) with the highest intensity at 28.96°. The fittings were performed using a pseudo-Voigt function. The crystallite size of our Li⁺ co-doped LZO:Er,Yb NPs calculated using the Debye-Scherer equation demonstrates a constant increase with increasing Li⁺ concentration (Table 1). The unit cell lattice constants calculated with the Bragg's equation according to XRD results for simple cubic system with *a* = *b* = *c* are also shown in Table 1.

3.3. Raman spectra

To have clear idea of the crystal structures of the Li⁺ co-doped LZO:Er,Yb NPs and the corresponding structural changes induced by Li⁺ co-doping, we have also taken their Raman spectra (Fig. 2b). Upon Li⁺ co-doping, the Raman spectra become a single broad band from a well-resolved sextet in a range of 200–1000 cm⁻¹, which is a clear indication of phase transition from the OP to DF structure [30]. During the initial concentration up to 2% Li⁺ co-doping, a few signatures of the OP structure persist with a large fraction of the DF phase. At 5% Li⁺ co-doping, the structure completely transforms into the DF phase. This is the reason why the increase of UC intensity is less evident at 1% and 2% Li⁺ co-doping levels whereas the maximum enhancement was observed at 5% Li⁺ co-doping level. The DF phase has only one broad Raman active *T*_{2g} mode which is assigned to internal La–O stretching mode [46]. Doping induced phase transition of inorganic matrices by ions (e.g. Li, U, Eu, etc.) has previously been observed by us and many other groups [6, 28, 47, 48].

When Li⁺ ions are co-doped into the LZO lattice and occupies the La³⁺ sites, charge balance most likely proceeds via the formation of two antisite defects as discussed in the following equation [49]:



However, the formation of oxygen vacancies on Li⁺ co-doping cannot be completely ruled out as it has been reported to happen at low Li⁺ co-doping level [12, 17]. At high Li⁺ co-doping level, Li⁺ ions at both substitutional and interstitial sites can co-exist as reported [49].

Based on the closeness of ionic radius of La³⁺ and Zr⁴⁺ ions, Li⁺ ions should occupy both La³⁺ and Zr⁴⁺ sites (*r*_{Li⁺} = 76 pm and *r*_{Zr⁴⁺} = 72 pm). This substitution invokes the need for charge compensating defects. In the LZO host, the chances to form oxygen vacancies by Li⁺ co-doping are achieved through equations (3) and (4) if occupying La³⁺ and Zr⁴⁺ sites, respectively:

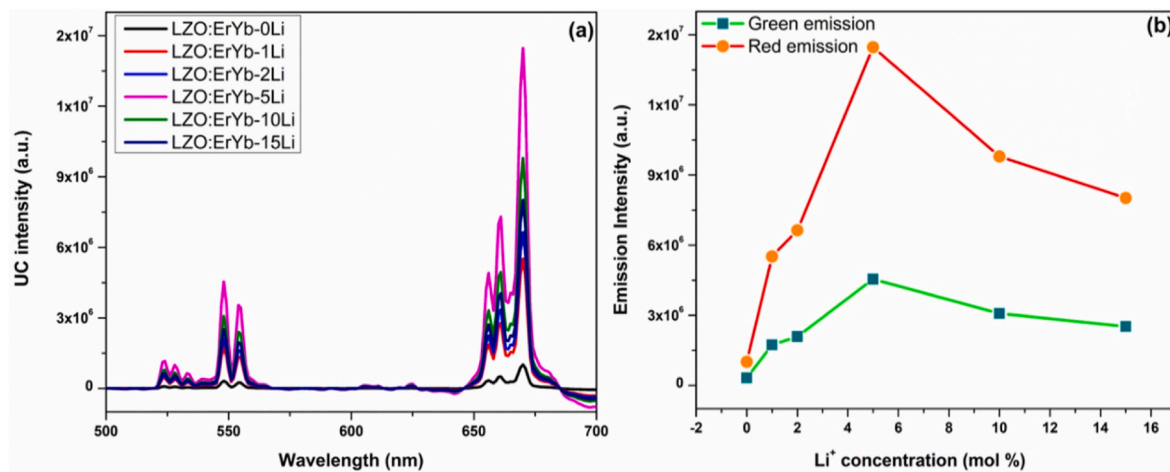
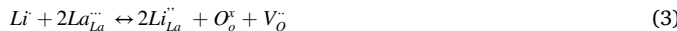


Fig. 3. (a) UC emission spectra of the LZO:Er,Yb NPs co-doped with different Li⁺ concentrations and (b) the corresponding intensity variations of the green and red UC emissions as a function of Li⁺ co-doping level. (For interpretation of the references to color in this figure legend, the reader is referred to the Web version of this article.)



As a result of the aliovalent doping, positively charged oxygen vacancies are formed which can distort the basic structural network of the LZO NPs.

Lighter electropositive ions such as Li⁺ ions have strong affinity towards distorted electron cloud which is induced by enhanced polarizability and thus favoring DF structure of the LZO host. This may be one of the probable reasons of the phase transition from OP to DF structure. Also, Li⁺ co-doped into the LZO host lattice may alter the electron charge density due to the charge mismatch and localization of Li⁺ ion (76 pm) at smaller Zr⁴⁺ (72 pm) or larger La³⁺ (116 pm) site, causing significant distortion in electron cloud in the LZO crystal lattice which may ultimately deform the crystal lattice [50]. Additional distortion will be accused by the formation of oxygen vacancies as a result of Li⁺ ion occupying either La³⁺ or Zr⁴⁺ site via equations (3) and (4). Such modification of crystal lattice may lead to the formation of irregular and DF structured LZO:Er,Yb NPs. Moreover, the presence of these oxygen vacancies, antisite and interstitial defects may have reduced the material's density and therefore the crystallite size expands.

3.4. Improving UC intensity by Li co-doping

The UC emission spectra of the LZO:3%Er³⁺,20%Yb³⁺ NPs with different Li⁺ co-doping concentrations (Fig. 3a) display three different regions: two green bands in the ranges of 520–540 nm and 545–565 nm and an intense red band spanning through 652–674 nm. These emissions are ascribed to ²H_{11/2}→⁴I_{15/2}, ⁴S_{3/2}→⁴I_{15/2}, and ⁴F_{9/2}→⁴I_{15/2} transitions of Er³⁺ ions, respectively.

More importantly, the green and red UC emissions have been distinctly enhanced with Li⁺ co-doping (Fig. 3b). As a function of Li⁺ co-doping concentration, UC intensity initially increases up to 5% of co-doped Li⁺ ions. After that, the UC intensity of both the green and red bands gradually decreases while still higher than that of the LZO:ErYb-0Li NPs. Compared to the LZO:ErYb-0Li NPs, the largest UC enhancement of the green and red bands was observed from the LZO:ErYb-5Li NPs, which was about 14- and 18-fold, respectively. These results are comparable to those reported for the most explored UC material, i.e., NaYF₄:Er,Yb. Specifically, Du et al. enhanced the UC intensities of the green and red emissions of their NaYF₄:Er,Yb NPs by Cu²⁺ induced phase transition for 37 and 25 times, respectively [2]. Nannuri et al. enhanced the UC intensities of the green and red emissions of their NaYF₄:Er,Yb samples by thermally induced phase transition for 24 and 33 times, respectively [3].

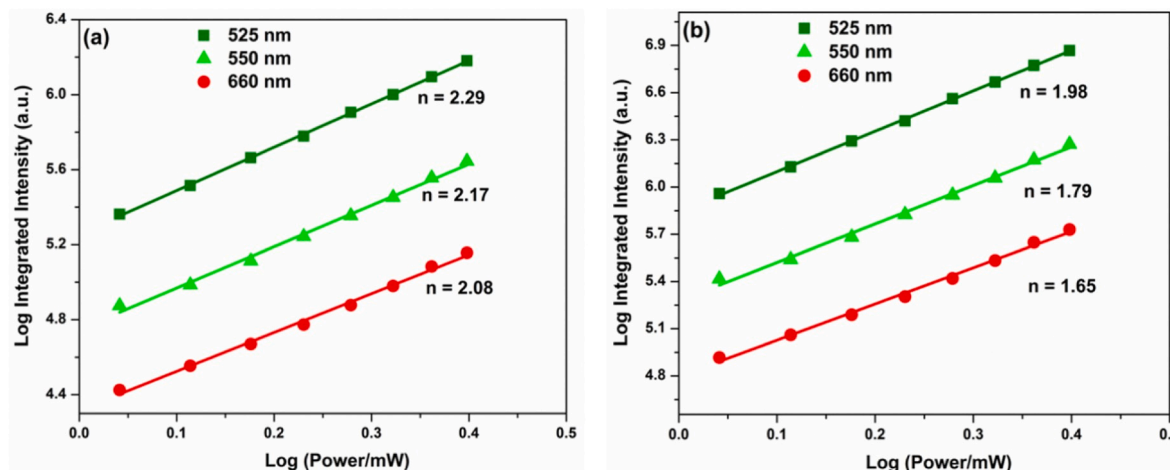


Fig. 4. Laser power dependence of the green and red emissions from the LZO:Er,Yb NPs (a) without Li⁺ co-doping and (b) with 5% Li⁺ co-doping. (For interpretation of the references to color in this figure legend, the reader is referred to the Web version of this article.)

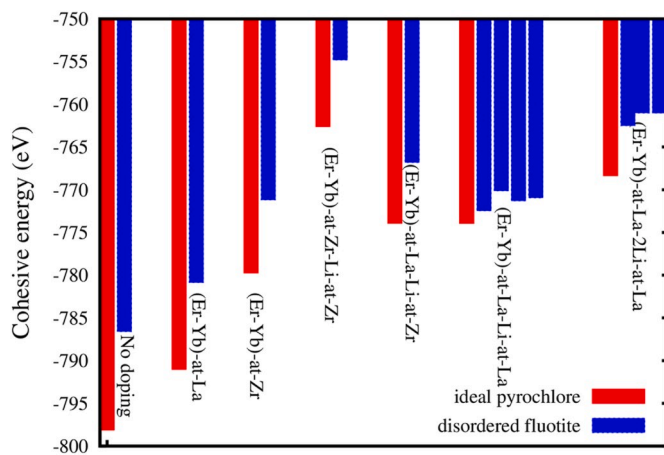


Fig. 5. A comparison of GGA calculated cohesive energies (for an 88-atom supercell) of OP and DF of the LZO host with (a) no doping, (b) one atom of (Er + Yb) each doped at La site, (c) one atom of (Er + Yb) each doped at Zr site, (d) one atom of (Er + Yb) each doped at La-site and one Li atom co-doped at Zr site, (e) one atom of (Er + Yb) each doped at La-site and one Li atom co-doped at La site, (f) one atom of (Er + Yb) each doped at Zr site and Li co-doped at Zr site, and (g) one atom of (Er + Yb) each doped and two Li atoms co-doped at La site.

As discussed previously, Raman spectral of our LZO:Er,Yb NPs (Fig. 2b) clearly confirmed the phase transition from the OP to DF structure upon Li^+ co-doping. Such order-disorder phase transition of the LZO crystal lattice may cause a local symmetry reduction of the crystalline field around the activator Er^{3+} ions [30]. This symmetry

reduction relaxes the Laporte forbidden transition of lanthanide ions, which make the intramolecular f-f transition allowed and the energy transfer from sensitizing Yb^{3+} ions to activator Er^{3+} ions favorable in terms of efficiency and rate [51]. There are other possible reasons for the UC enhancement, such as the modifications of crystal field and local symmetry by Li^+ co-doping. Our XRD data have inferred that Li^+ ions are localized at $\text{La}^{3+}/\text{Zr}^{4+}$ lattice sites up to 5% co-doping level. At higher than 5% co-doping level, Li^+ ions are incorporated into interstitial positions which generate rich defect centers. These defects reduce UC intensity by providing non-radiative pathways. Our observations are in good agreement with previous reports [14,24,43,45].

To determine the number of photons responsible for the UC emission from the LZO:Er,Yb NPs co-doped with different concentrations of Li^+ ions, the UC intensity was measured as a function of the pump power using the LZO:Er,Yb NPs without Li^+ co-doping and with 5% Li^+ co-doping (Fig. 4). To interpret the number of photons required to populate the upper emitting states, the relationship was fitted by the following equation:

$$I \propto P^n \quad (5)$$

where I is the fluorescent UC intensity, P is the laser power, and n is the number of pump photons required. Based on the fitting, the obtained slopes corresponding to the n values were 1.98, 1.79 and 1.65 for the 525, 550 and 660 nm emissions of the LZO:Er,Yb NPs co-doped with 5% Li^+ (Fig. 4b), which are slightly smaller than those n values of the LZO:Er,Yb NPs without Li^+ co-doping (Fig. 4a). These results indicate that the green and red emissions from these NPs are two-photon processes no matter with Li^+ co-doping or not. Li^+ ions cannot absorb 980 nm photons and therefore no energy transfer to activator Er^{3+} ions. In other words, the UC emission mechanism of our LZO:Er,Yb NPs is not affected

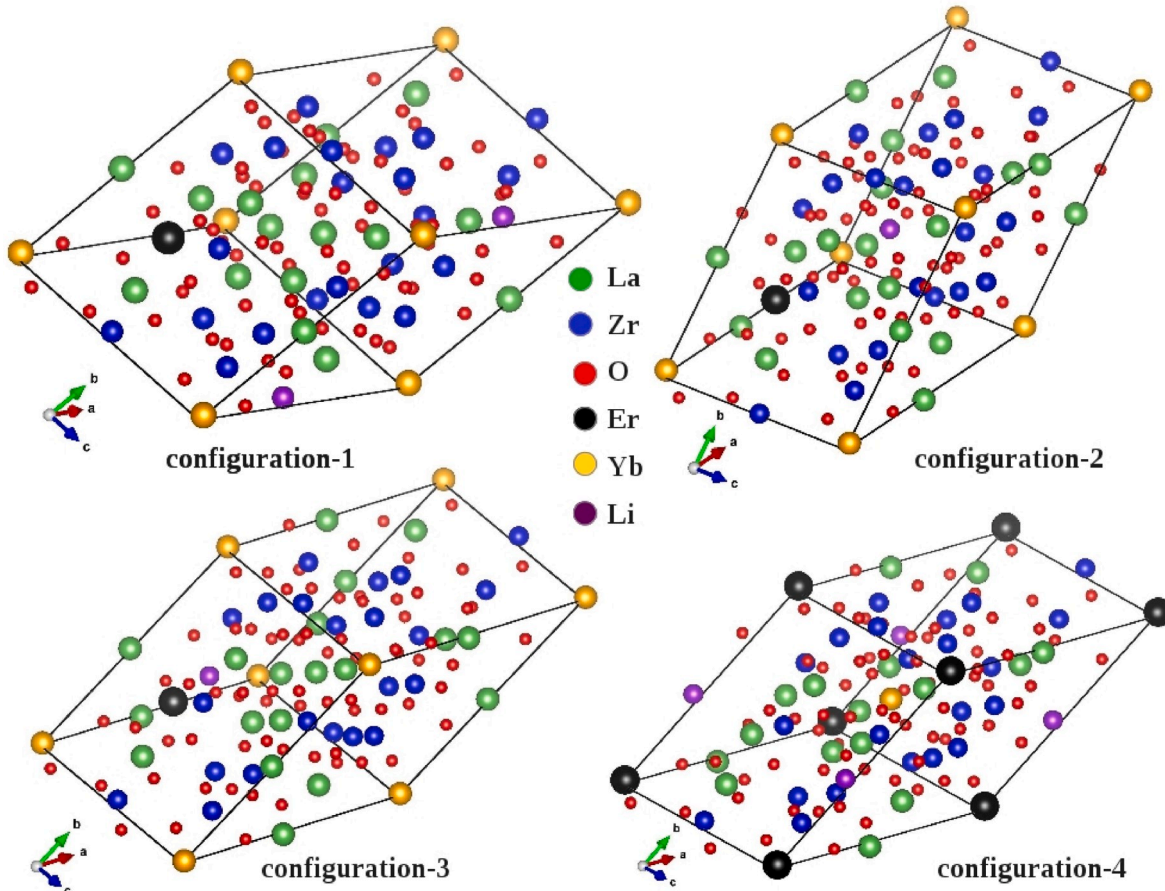


Fig. 6. Different configurations of Li^+ co-doping compared to (Er + Yb) doping at La sites in the DF structure of LZO.

Table 2

DFT-GGA calculated cohesive energies of the OP and DF structures of LZO host (with no-doping, (Er + Yb)-doped, and (Er + Yb) + Li-co-doped) are tabulated with respect to the most stable structure. The DF and OP energy difference values are reported for the 88-atom supercell.

Configuration	$E(\text{DF})-E(\text{OP})$ (eV/atom)	Li-Er/Li-Yb bond length in DF
No doping	0.131	
Er + Yb doped at La site	0.116	
Er + Yb doped at Zr site	0.097	
Er + Yb doped and Li co-doped at Zr site:		
configuration 1	0.089	Er-Li = 9.36 Å, Yb-Li = 7.80 Å
configuration 2	0.088	Er-Li = 12.58 Å, Yb-Li = 9.98 Å
configuration 3	0.082	Er-Li = 3.64 Å, Yb-Li = 6.76 Å
configuration 4	0.085	Er-Li = 7.55 Å, Yb-Li = 3.26 Å
configuration5	0.069	Er-Li = 6.81 Å, Yb-Li = 7.47 Å
Er + Yb doped at La site and Li co-doped at Zr site:		
configuration 1	0.081	Er-Li = 8.07 Å, Yb-Li = 5.86 Å
configuration 2	0.079	Er-Li = 7.63 Å, Yb-Li = 5.83 Å
configuration 3	0.082	Er-Li = 3.22 Å, Yb-Li = 3.40 Å
configuration 4	0.640	Er-Li = 3.28 Å, Yb-Li = 7.09 Å
Er + Yb doped at La site and one Li atom co-doped at La site:		
configuration 1	0.016	Er-Li = 4.46 Å, Yb-Li = 5.94 Å
configuration 2	0.030	Er-Li = 3.06 Å, Yb-Li = 5.96 Å
configuration 3	0.034	Er-Li = 5.66 Å, Yb-Li = 7.85 Å
configuration 4	0.043	Er-Li = 6.44 Å, Yb-Li = 7.28 Å
Er + Yb doped at La site and two Li atom co-doped at La site:		
configuration 1	0.066	Er-Li1 = 3.56 Å, Yb-Li1 = 6.08 Å Er-Li2 = 3.26 Å, Yb-Li2 = 5.66 Å Er-Li1 = 9.59 Å, Yb-Li1 = 5.77 Å Er-Li2 = 6.34 Å, Yb-Li2 = 7.24 Å Er-Li1 = 4.40 Å, Yb-Li1 = 5.34 Å Er-Li2 = 3.81 Å, Yb-Li2 = 5.15 Å
configuration 2	0.083	
configuration 3	0.083	

by the introduction of Li^+ ions.

3.5. DFT calculations

To further understand the underlying reasons for the observed enhanced UC performance of our LZO:Er,Yb NPs co-doped with Li^+ and the relevant phase transition, we aim to show how the structural stability of the OP and DF phases changes with respect to (Er + Yb) doping and Li co-doping in the LZO host based on DFT calculated cohesive energies. For this purpose, a comparison of the DFT-GGA calculated cohesive energies of the OP and DF structures of LZO was made in the following seven configurations: (a) no doping, (b) one atom of (Er + Yb) each doped at La site, (c) one atom of (Er + Yb) each doped at Zr site, (d) one atom of (Er + Yb) each doped at La-site and one Li atom co-doped at Zr site, (e) one atom of (Er + Yb) each doped at La-site and one Li atom co-doped at La site, (f) one atom of (Er + Yb) each doped at Zr site and Li co-doped at Zr site, and (g) one atom of (Er + Yb) each doped and two Li atoms co-doped at La site (Fig. 5 and Table 2). These seven configurations depict possible distribution of (Er + Yb) and Li atoms at La and Zr sites of the LZO host such that the DF structure became energetically favorable (or close to this) over the OP structure as experimentally demonstrated above.

In all calculations, the total number of atoms were 88 in a supercell. Fig. 5 and Table 2 show the energy differences of the OP and DF structures reduces due to doping of Er and Yb atoms (in 1/16 concentration each) at both La and Zr sites. This difference further reduces with Li co-doping (1/16 concentration) at La and Zr sites. The cohesive energy differences become as small as 16 meV/atom in the case of (Er + Yb) doped and Li co-doped both at La site. This small energy difference is of the order of vibrational energy of atoms at 300 K (26 meV/atom). As a result, the DF structure may become energetically favorable at room temperature with (Er + Yb) doping and Li co-doping. The Li co-doping at Zr site reduces the cohesive energy differences between (Er + Yb) doped OP and DF structures, but the energy differences is almost 5 times more than the case of Li co-doping at La site. As there could be various configurations in which (Er + Yb) doping and Li co-doping can be done in the DF structure, the relative energy differences of those configurations

may also differ. In order to confirm that the DFT calculated energy stability sequence does not change with the positioning of the Li co-doping in the (Er + Yb) doped LZO, several configurations were made with varying Li-Er/Li-Yb bond lengths as shown in Table 2 and Fig. 6. In all these calculations the position of (Er + Yb) atoms were kept fixed in the DF structures. Our test calculations showed that Li atom position greater than 10 Å with respect to the (Er + Yb) atoms has insignificant effect on the $E(\text{DF})-E(\text{OP})$.

Specifically, for the case of Li co-doped at La site, 4 different configurations of Li co-doping were considered based on Li atom distance from Er/Yb atom (as shown in Fig. 6). The energy variation of Li-co-doped structures are listed in Table 2 along with Li-Er and Li-Yb bond distances. Table 2 shows that with an optimum distance of Li-Er/Li-Yb bond (4.46/5.94 Å), configuration 1 is the most energetically favorable structure compared to other configurations. The configurations with Li position having shorter and/or longer Li-Er bond distances than configuration 1 has higher energy differences $E(\text{DF})-E(\text{OP})$ implying less stability of the DF structure compared to the OP structure. In other configurations, this energy difference is almost 2–3 times higher than that of configuration 1. This means positioning of Li atoms with respect to Er/Yb doping site has significant effect on relative stability of the DF and OP structures. Table 2 also shows the energy differences of DF and OP with two Li atoms co-doping (2/16 Li concentration at La site). With increased Li concentration, the $E(\text{DF})-E(\text{OP})$ has increased by 4–5 times compared to the most stable configuration of the singly Li co-doped case. This implies that increased Li concentration at La site destabilizes the DF structure compared to the OP structure. Hence, there is a limit of Li incorporation at La site.

4. Conclusion

In this work, we observed an order-disorder structural phase transition of the LZO:Er,Yb NPs by Li^+ co-doping. The Li^+ co-doping level varied from 0% to 15%. Also, we studied the influence of Li^+ co-doping to the $\text{La}_2\text{Zr}_2\text{O}_7:3\%\text{Er}^{3+}, 20\%\text{Yb}^{3+}$ nanoparticles on their upconversion intensity. Once optimally co-doped with 5mol% Li^+ ions, a significant increase of the UC emission intensity was observed, specifically, by 14–

and 18-fold of the green and red UC emissions, respectively. Such enhancement is attributed to the reduction of local symmetry around Er^{3+} ions. This relaxes the selection rule and allows faster energy transfer while the number of photon absorption in the UC process does not change upon Li^+ co-doping. DFT studies on these NPs supported our experimental results that Li^+ co-doping favors the DF structure in the LZO NPs. Based on DFT calculations, it was also inferred that the DF structure might become energetically favorable at room temperature with (Er + Yb) doping and Li co-doping. Moreover, DFT calculations pinpointed the fact that the positioning of Li atoms with respect to Er doping site has a significant effect on the relative stability of the DF and OP structures. The configuration wherein the lithium-erbium bond with a bond length of 4.46 Å is the most energetically favorable structure compared to other configurations. Overall, we proposed a new design strategy to enhance UC luminescence intensity by inducing structural phase transition through Li^+ co-doping. This strategy can be applied to other low phonon energy hosts to achieve their possible implications in a more significant ways in the future.

CRediT authorship contribution statement

Santosh K. Gupta: Conceptualization, Data curation, Formal analysis, Methodology, Writing - original draft. **Maya Abdou:** Data curation. **Jose P. Zuniga:** Data curation. **Partha S. Ghosh:** Data curation, Formal analysis, Writing - original draft. **Yuanbing Mao:** Conceptualization, Formal analysis, Methodology, Supervision, Writing - review & editing.

Acknowledgement

YM would like to thank the financial support by the National Science Foundation under CHE (award #17110160) and the IIT startup funds. SKG thanks the United States-India Education Foundation (USIEF, India) and the Institute of International Education (IIE, USA) for his Fulbright Nehru Postdoctoral Fellowship (Award# 2268/FNPDR/2017).

References

- Y. Chen, Z. Wang, S. Chen, H. Ren, B. Li, W. Yan, et al., Electric-field control of Li-doping induced phase transition in VO_2 film with crystal facet-dependence, *Nanomater. Energy* 51 (2018) 300–307.
- K. Du, X. Xu, S. Yao, P. Lei, L. Dong, M. Zhang, et al., Enhanced upconversion luminescence and controllable phase/shape of $\text{NaYF}_4\text{:Yb}/\text{Er}$ crystals through Cu^{2+} ion doping, *CrystEngComm* 20 (14) (2018) 1945–1953.
- S.H. Nannuri, S.D. Kulkarni, KSC, S. Chidangil, S.D. George, Post annealing induced manipulation of phase and upconversion luminescence of Cr^{3+} doped $\text{NaYF}_4\text{:Yb},\text{Er}$ crystals, *RSC Adv.* 9 (17) (2019) 9364–9372.
- Y. Shang, S. Hao, J. Liu, M. Tan, N. Wang, C. Yang, et al., Synthesis of upconversion $\beta\text{-NaYF}_4\text{:Nd}^{3+}/\text{Yb}^{3+}/\text{Er}^{3+}$ particles with enhanced luminescent intensity through control of morphology and phase, *Nanomaterials* 5 (1) (2015) 218–232.
- G. Tian, Z. Gu, L. Zhou, W. Yin, X. Liu, L. Yan, et al., Mn^{2+} dopant-controlled synthesis of $\text{NaYF}_4\text{:Yb}/\text{Er}$ upconversion nanoparticles for in vivo imaging and drug delivery, *Adv. Mater.* 24 (9) (2012) 1226–1231.
- G. Viola, R. McKinnon, V. Koval, A. Adomkevicius, S. Dunn, H. Yan, Lithium-induced phase transitions in lead-free $\text{Bi}_{0.5}\text{Na}_{0.5}\text{TiO}_3$ based ceramics, *J. Phys. Chem. C* 118 (16) (2014) 8564–8570.
- X. Xu, Z. Wang, P. Lei, X. Liu, Y. Su, L. Dong, et al., Cubic $\text{KLu}_3\text{F}_{10}$ nanocrystals: Mn^{2+} dopant-controlled synthesis and upconversion luminescence, *Dalton Trans.* 44 (39) (2015) 17286–17292.
- X. Xu, X. Zhai, K. Du, P. Lei, L. Dong, R. Deng, et al., The size-responsive phase transition mechanism and upconversion/downshifting luminescence properties of $\text{KLu}_2\text{F}_7\text{:Yb}^{3+}/\text{Er}^{3+}$ nanocrystals, *J. Mater. Chem. C* 5 (25) (2017) 6311–6318.
- S. Wagner, P. Klose, V. Burlaka, K. Nöthemann, M. Hamm, A. Pundt, Structural phase transitions in niobium hydrogen thin films: mechanical stress, phase equilibria and critical temperatures, *ChemPhysChem* 20 (14) (2019) 1890–1904.
- B.W. Boote, H.P. Andaraarachchi, B.A. Rosales, R. Blome-Fernández, F. Zhu, M. D. Reichert, et al., Unveiling the photo- and thermal-stability of cesium lead halide perovskite nanocrystals, *ChemPhysChem* 20 (20) (2019) 2647–2656.
- S.K. Gupta, K. Sudarshan, A.K. Yadav, R. Gupta, D. Bhattacharyya, S.N. Jha, et al., Deciphering the role of charge compensator in optical properties of $\text{SrWO}_4\text{:Eu}^{3+}\text{:A}$ ($\text{A} = \text{Li}^+, \text{Na}^+, \text{K}^+$): spectroscopic insight using photoluminescence, positron annihilation, and X-ray absorption, *Inorg. Chem.* 57 (2) (2018) 821–832.
- N. Dhananjaya, H. Nagabhushana, B.M. Nagabhushana, B. Rudraswamy, C. Shivakumara, R.P.S. Chakradhar, Effect of Li^+ -ion on enhancement of photoluminescence in $\text{Gd}_2\text{O}_3\text{:Eu}^{3+}$ nanophosphors prepared by combustion technique, *J. Alloys Compd.* 509 (5) (2011) 2368–2374.
- B.P. Singh, A.K. Parchur, R.S. Ningthoujam, P.V. Ramakrishna, S. Singh, P. Singh, et al., Enhanced up-conversion and temperature-sensing behaviour of Er^{3+} and Yb^{3+} co-doped $\text{Y}_2\text{Ti}_2\text{O}_7$ by incorporation of Li^+ ions, *Phys. Chem. Chem. Phys.* 16 (41) (2014) 22665–22676.
- C. Zhao, X. Kong, X. Liu, L. Tu, F. Wu, Y. Zhang, et al., Li^+ ion doping: an approach for improving the crystallinity and upconversion emissions of $\text{NaYF}_4\text{:Yb}^{3+},\text{Tm}^{3+}$ nanoparticles, *Nanoscale* 5 (17) (2013) 8084–8089.
- W. Yin, L. Zhao, L. Zhou^o, Z. Gu, X. Liu, G. Tian^o, et al., Enhanced red emission from $\text{GdF}_3\text{:Yb}^{3+},\text{Er}^{3+}$ upconversion nanocrystals by Li^+ doping and their application for bioimaging, *Chem. Eur. J.* 18 (30) (2012) 9239–9245.
- S.P. Tiwari, S.K. Maurya, R.S. Yadav, A. Kumar, V. Kumar, M.-F. Joubert, et al., Future prospects of fluoride based upconversion nanoparticles for emerging applications in biomedical and energy harvesting, *Journal of Vacuum Science & Technology B, Nanotechnology and Microelectronics: Materials, Processing, Measurement, and Phenomena* 36 (6) (2018), 060801.
- I. Hyppänen, N. Perälä, R. Arppe, M. Schäferling, T. Soukka, Environmental and excitation power effects on the ratiometric upconversion luminescence based temperature sensing using nanocrystalline $\text{NaYF}_4\text{:Yb}^{3+}, \text{Er}^{3+}$, *ChemPhysChem* 18 (6) (2017) 692–701.
- L. Gemini, T. Schmitz, R. Kling, S. Barcikowski, B. Gökce, Upconversion nanoparticles synthesized by ultrashort pulsed laser ablation in liquid: effect of the stabilizing environment, *ChemPhysChem* 18 (9) (2017) 1210–1216.
- C. Sorbello, P. Gross, C.A. Strassert, M. Jobbág, B.C. Barja, $\text{Ce}^{IV}\text{-Gd}^{III}$ mixed oxides as hosts for Er^{III} -based upconversion phosphors, *ChemPhysChem* 18 (10) (2017) 1407–1414.
- Q.-C. Sun, Y.C. Ding, D.M. Sagar, P. Nagpal, Photon upconversion towards applications in energy conversion and bioimaging, *Prog. Surf. Sci.* 92 (4) (2017) 281–316.
- S. Wen, J. Zhou, K. Zheng, A. Bednarkiewicz, X. Liu, D. Jin, Advances in highly doped upconversion nanoparticles, *Nat. Commun.* 9 (1) (2018) 2415.
- Y. Sun, X. An, L. Chen, Q. Gao, X. Zhang, L. Duan, et al., Upconverting nanophosphor incorporated photoanodes for improved photoelectric performances of quantum dot sensitized solar cells, *Materials Research Letters* 6 (6) (2018) 314–320.
- Q. Huang, J. Yu, E. Ma, K. Lin, Synthesis and characterization of highly efficient near-infrared upconversion $\text{Sc}^{3+}/\text{Er}^{3+}/\text{Yb}^{3+}$ tridoped NaYF_4 , *J. Phys. Chem. C* 114 (10) (2010) 4719–4724.
- Q. Cheng, J. Stui, W. Cai, Enhanced upconversion emission in Yb^{3+} and Er^{3+} codoped NaGdF_4 nanocrystals by introducing Li^+ ions, *Nanoscale* 4 (3) (2012) 779–784.
- A. Kar, S. Kundu, A. Patra, Lanthanide-doped nanocrystals: strategies for improving the efficiency of upconversion emission and their physical understanding, *ChemPhysChem* 16 (3) (2015) 505–521.
- R.A. Hansel, S.K. Desai, S.W. Allison, A.L. Heyes, D.G. Walker, Emission lifetimes of europium-doped pyrochlores for phosphor thermometry, *J. Appl. Phys.* 107 (1) (2010), 016101.
- S.K. Gupta, M. Abdou, J.P. Zuniga, P.S. Ghosh, E. Molina, B. Xu, et al., Roles of oxygen vacancies and pH induced size changes on photo- and radioluminescence of undoped and Eu^{3+} -doped $\text{La}_2\text{Zr}_2\text{O}_7$ nanoparticles, *J. Lumin.* 209 (2019) 302–315.
- M. Abdou, S.K. Gupta, J.P. Zuniga, Y. Mao, On structure and phase transformation of uranium doped $\text{La}_2\text{Hf}_2\text{O}_7$ nanoparticles as an efficient nuclear waste host, *Materials Chemistry Frontiers* 2 (12) (2018) 2201–2211.
- K.A. Sakharov, E.P. Simonenko, N.P. Simonenko, M.L. Vaganova, Y.E. Lebedeva, A. S. Chaynikova, et al., Glycol-citrate synthesis of fine-grained oxides $\text{La}_{2-x}\text{Gd}_x\text{Zr}_2\text{O}_7$ and preparation of corresponding ceramics using FAST/SPS process, *Ceram. Int.* 44 (7) (2018) 7647–7655.
- S.K. Gupta, M. Abdou, P.S. Ghosh, J.P. Zuniga, Y. Mao, Thermally induced disorder-order phase transition of $\text{Gd}_2\text{Hf}_2\text{O}_7\text{:Eu}^{3+}$ nanoparticles and its implication on photo- and radioluminescence, *ACS Omega* 4 (2) (2019) 2779–2791.
- S. Zhang, H.B. Zhang, F.A. Zhao, M. Jiang, H.Y. Xiao, Z.J. Liu, et al., Impact of isovalent and aliovalent substitution on the mechanical and thermal properties of $\text{Gd}_2\text{Zr}_2\text{O}_7$, *Sci. Rep.* 7 (1) (2017) 6399.
- F. Yang, Y. Wang, X. Zhao, P. Xiao, Enhanced ionic conductivity in pyrochlore and fluorite mixed phase yttrium-doped lanthanum zirconate, *J. Power Sources* 273 (2015) 290–297.
- F. Zhong, J. Zhao, L. Shi, Y. Xiao, G. Cai, Y. Zheng, et al., Alkaline-earth metals-doped pyrochlore $\text{Gd}_2\text{Zr}_2\text{O}_7$ as oxygen conductors for improved NO_2 sensing performance, *Sci. Rep.* 7 (1) (2017) 4684.
- P.M. Marley, G.A. Horrocks, K.E. Pelcher, S. Banerjee, Transformers: the changing phases of low-dimensional vanadium oxide bronzes, *Chem. Commun.* 51 (25) (2015) 5181–5198.
- S.K. Gupta, M.A.P. Garcia, J.P. Zuniga, M. Abdou, Y. Mao, Visible and ultraviolet upconversion and near infrared downconversion luminescence from lanthanide doped $\text{La}_2\text{Zr}_2\text{O}_7$ nanoparticles, *J. Lumin.* 214 (2019) 116591.
- G. Kresse, J. Furthmüller, Efficient iterative schemes for ab initio total-energy calculations using a plane-wave basis set, *Phys. Rev. B* 54 (16) (1996) 11169.
- G. Kresse, J. Furthmüller, Efficiency of ab-initio total energy calculations for metals and semiconductors using a plane-wave basis set, *Comput. Mater. Sci.* 6 (1) (1996) 15–50.
- P.E. Blöchl, Projector augmented-wave method, *Phys. Rev. B* 50 (24) (1994) 17953.
- J.P. Perdew, K. Burke, M. Ernzerhof, Generalized gradient approximation made simple, *Phys. Rev. Lett.* 77 (18) (1996) 3865.
- H.J. Monkhorst, J.D. Pack, Special points for Brillouin-zone integrations, *Phys. Rev. B* 13 (12) (1976) 5188.

[41] P.E. Blöchl, O. Jepsen, O.K. Andersen, Improved tetrahedron method for Brillouin-zone integrations, *Phys. Rev. B* 49 (23) (1994) 16223.

[42] C. Jiang, C. Stanek, K. Sickafus, B. Uberuaga, First-principles prediction of disordering tendencies in pyrochlore oxides, *Phys. Rev. B* 79 (10) (2009) 104203.

[43] H. Lin, D. Xu, D. Teng, S. Yang, Y. Zhang, Simultaneous size and luminescence control of $\text{NaYF}_4:\text{Yb}^{3+}/\text{RE}^{3+}$ ($\text{RE} = \text{Tm, Ho}$) microcrystals via Li^+ doping, *Opt. Mater.* 45 (2015) 229–234.

[44] F. Wang, Y. Han, C.S. Lim, Y. Lu, J. Wang, J. Xu, et al., Simultaneous phase and size control of upconversion nanocrystals through lanthanide doping, *Nature* 463 (2010) 1061.

[45] J.H. Kim, H. Choi, E.O. Kim, H.M. Noh, B.K. Moon, J.H. Jeong, Li doping effects on the upconversion luminescence of $\text{Yb}^{3+}/\text{Er}^{3+}$ -doped ABO_4 ($\text{A} = \text{Ca, Sr}$; $\text{B} = \text{W, Mo}$ phosphors, *Opt. Mater.* 38 (2014) 113–118.

[46] M. Abdou, S.K. Gupta, J.P. Zuniga, Y. Mao, Insight into the effect of A-site cations on structural and optical properties of $\text{RE}_2\text{Hf}_2\text{O}_7:\text{U}$ nanoparticles, *J. Lumin.* 210 (2019) 425–434.

[47] S.K. Gupta, K. Sudarshan, P.S. Ghosh, S. Mukherjee, R.M. Kadam, Doping-induced room temperature stabilization of metastable $\beta\text{-Ag}_2\text{WO}_4$ and origin of visible emission in α - and $\beta\text{-Ag}_2\text{WO}_4$: low temperature photoluminescence studies, *J. Phys. Chem. C* 120 (13) (2016) 7265–7276.

[48] X. Zhang, H. Yu, L. Guo, J. Jin, Q. Li, Y. Guo, et al., Comprehensive model and investigation of F^- ions-induced cubic-to-hexagonal phase transformation in NaYF_4 , *J. Alloys Compd.* 728 (2017) 1254–1259.

[49] R. Mani, S.K. Gupta, P.S. Ghosh, H. Jiang, Yellow emission from low coordination site of $\text{Sr}_2\text{SiO}_4:\text{Eu}^{2+},\text{Ce}^{3+}$: influence of lanthanide dopants on the electron density and crystallinity in crystal site engineering approach, *Chem. Eur. J.* 24 (60) (2018) 16149–16159.

[50] H. Lin, D. Xu, A. Li, L. Yao, Z. Qiu, S. Yang, et al., Facile synthesis and emission enhancement in NaLuF_4 upconversion nano/micro-crystals via Y^{3+} doping, *Sci. Rep.* 7 (1) (2017) 13762.

[51] X. Chen, Z. Liu, Q. Sun, M. Ye, F. Wang, Upconversion emission enhancement in $\text{Er}^{3+}/\text{Yb}^{3+}$ -codoped BaTiO_3 nanocrystals by tridoping with Li^+ ions, *Optic Commun.* 284 (7) (2011) 2046–2049.